Supporting Information for "Numerical dynamo simulations reproduce palaeomagnetic field behaviour"

D. G. Meduri[1], A. J. Biggin[1], C. J. Davies[2], R. K. Bono[1], C. J. Sprain[3],

J. Wicht[4]

[1]Department of Earth, Ocean and Ecological Sciences, University of Liverpool, Liverpool, UK

[2]School of Earth and Environment, University of Leeds, Leeds, UK

[3]Department of Geological Sciences, University of Florida, Gainesville, FL, USA

[4]Department Planets and Comets, Max Planck Institute for Solar System Research, Göttingen, Germany

Contents of this file

1. Section S1: Numerical Geodynamo Models

2. Figures S1 to S4

3. Tables S2 to S4

Additional Supporting Information (Files uploaded separately)

1. Captions for large Tables S1 and S5

Corresponding author: D. G. Meduri, Department of Earth, Ocean and Ecological Sciences, University of Liverpool, Liverpool, UK. (domenico.meduri@liverpool.ac.uk)

S1. Numerical Geodynamo Models

Here we provide further details on the numerical geodynamo models outlined in Section 2.1. The dimensionless equations governing the system are: the momentum equation

$$\frac{\mathrm{Ek}}{\mathrm{Pm}}\left[\frac{\partial \mathbf{u}}{\partial t}+(\mathbf{u}\cdot\nabla)\,\mathbf{u}\right]=-\nabla p-2\hat{\mathbf{e}}_z\times\mathbf{u}+\mathrm{Pm}\,\mathrm{Ra}\,\frac{C}{\alpha}\frac{r}{r_\mathrm{o}}\hat{\mathbf{e}}_r+\mathrm{Ek}\nabla^2\mathbf{u}+(\nabla\times\mathbf{B})\times\mathbf{B}, \quad (1)$$

the induction equation

$$\frac{\partial \mathbf{B}}{\partial t}=\nabla\times(\mathbf{u}\times\mathbf{B})+\nabla^2\mathbf{B}, \quad (2)$$

the equation of evolution for the codensity

$$\frac{\partial C}{\partial t}+(\mathbf{u}\cdot\nabla)\,C=\frac{\mathrm{Pm}}{\mathrm{Pr}}\,\nabla^2 C-\gamma, \quad (3)$$

the continuity equation

$$\nabla\cdot\mathbf{u}=0 \quad (4)$$

and the solenoidal condition for the magnetic induction

$$\nabla\cdot\mathbf{B}=0. \quad (5)$$

Here $\mathbf{u}$, $\mathbf{B}$ and p are the (dimensionless) fluid velocity, magnetic induction and a modified pressure which includes centrifugal forces, respectively. The codensity C can stand for αT or $\alpha\xi$, depending on whether thermal or chemical convection is considered. Here T (ξ) is the perturbation in temperature (light elements concentration) and α is the thermal (compositional) expansion coefficient. The radial spherical coordinate is r and $\hat{\mathbf{e}}_r$ and $\hat{\mathbf{e}}_z$ denote the unit vectors in the radial direction and along the rotation axis, respectively. The above equations are obtained using the shell thickness d as length scale and the magnetic diffusion time $t_\eta=d^2/\eta$ as time scale. The magnetic induction $\mathbf{B}$ is scaled by

$(\rho\mu_0\Omega\eta)^{1/2}$, where ρ is the reference fluid density and μ_0 the magnetic permeability of vacuum.

The dimensionless control parameters in the above equations are the Ekman number Ek, the Prandtl number Pr, the magnetic Prandtl number Pm (all defined in Section 2.1) and the Rayleigh number

$$\mathrm{Ra} = \frac{g_\mathrm{o}\Delta C d}{\Omega\nu}. \tag{6}$$

Here g_o is gravity at the outer boundary and ΔC is a codensity scale which depends on the convective driving mode. In thermally driven dynamos $\Delta C = \alpha\beta d$, where β is the conductive temperature gradient at the outer boundary. Thermal dynamos are purely bottom heated, hence $\gamma = 0$ in Equation (3). In chemical dynamos, the (dimensional) homogeneous sink term $-\tilde{\gamma}$ in the codensity transport equation serves to balance the codensity flux from the inner boundary. The codensity scale is $\Delta C = \tilde{\gamma} d^2/\eta$ so that $\gamma = 1$ in Equation (3).

Thermal dynamos were run using the numerical implementation of Willis, Sreenivasan, and Gubbins (2007) (further details on the code can be found in Davies et al., 2011). Simulations modelling chemical convection were performed using the code MagIC (Wicht, 2002; Schaeffer, 2013, available at `https://magic-sph.github.io`).

References

Davies, C. J., Gubbins, D., & Jimack, P. K. (2011). Scalability of pseudospectral methods for geodynamo simulations. *Concurrency and Computation: Practice and Experience*, *23*(1), 38–56. doi: 10.1002/cpe.1593

Ogg, J. (2012). Chapter 5 - Geomagnetic polarity time scale. In F. M. Gradstein,

J. G. Ogg, M. D. Schmitz, & G. M. Ogg (Eds.), *The geologic time scale* (pp. 85–113). Boston: Elsevier. doi: 10.1016/B978-0-444-59425-9.00005-6

Pozzo, M., Davies, C., Gubbins, D., & Alfè, D. (2012). Thermal and electrical conductivity of iron at Earth's core conditions. *Nature*, *485*, 355–358. doi: 10.1038/nature11031

Schaeffer, N. (2013). Efficient spherical harmonic transforms aimed at pseudospectral numerical simulations. *Geochemistry, Geophysics, Geosystems*, *14*(3), 751–758. doi: 10.1002/ggge.20071

Sprain, C. J., Biggin, A. J., Davies, C. J., Bono, R. K., & Meduri, D. G. (2019). An assessment of long duration geodynamo simulations using new paleomagnetic modeling criteria (Q_{PM}). *Earth and Planetary Science Letters*, *526*, 115758. doi: 10.1016/j.epsl.2019.115758

Wicht, J. (2002). Inner-core conductivity in numerical dynamo simulations. *Physics of the Earth and Planetary Interiors*, *132*(4), 281–302. doi: 10.1016/S0031-9201(02)00078-X

Wicht, J., & Meduri, D. G. (2016). A gaussian model for simulated geomagnetic field reversals. *Physics of the Earth and Planetary Interiors*, *259*, 45–60. doi: 10.1016/j.pepi.2016.07.007

Willis, A. P., Sreenivasan, B., & Gubbins, D. (2007). Thermal core-mantle interaction: Exploring regimes for "locked" dynamo action. *Physics of the Earth and Planetary Interiors*, *165*(1), 83–92. doi: 10.1016/j.pepi.2007.08.002

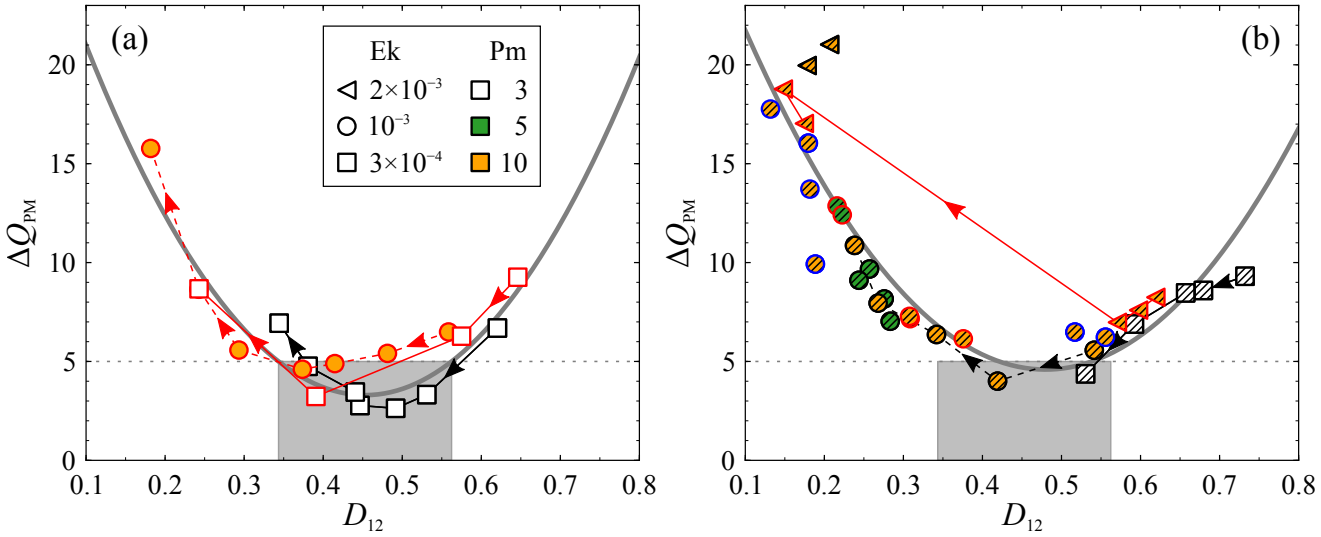

Figure S1: Same as Figure 1a,b but with the symbol colour coding the magnetic Prandtl number Pm. The simulation runs show no apparent dependency on Pm.

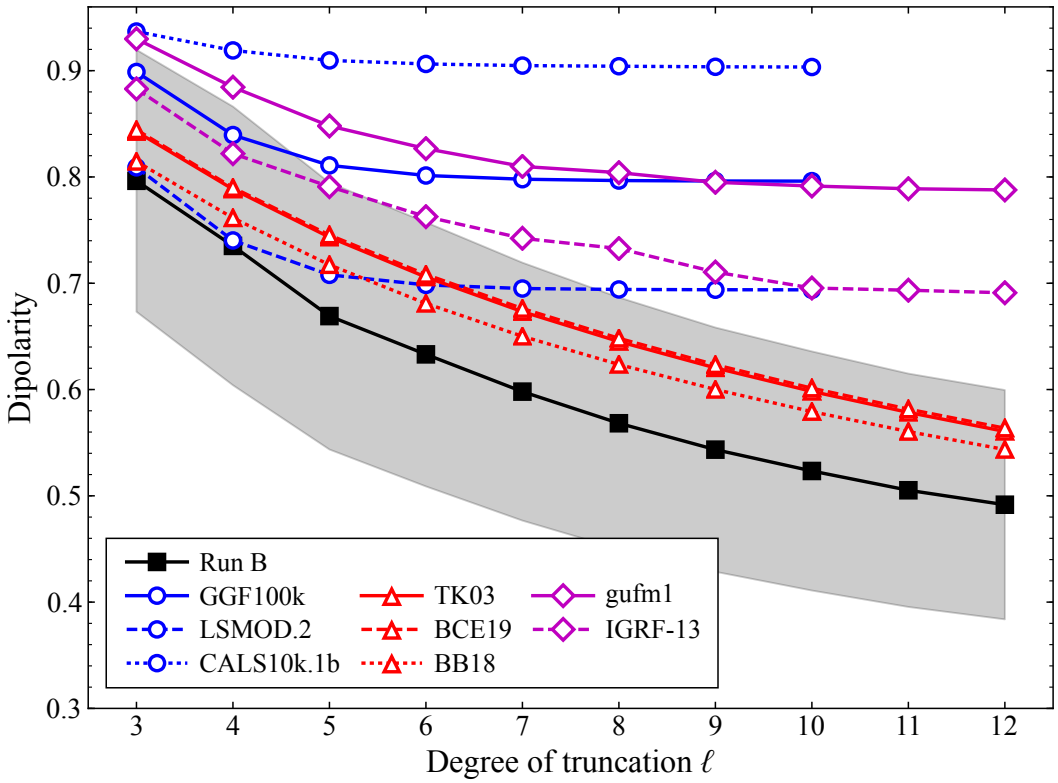

Figure S2: Dipolarity as a function of its spherical harmonic degree of truncation ($\ell = 4$ and $\ell = 12$ correspond to D_4 and D_{12} respectively). Connected squares show run B, our most palaeomagnetic-like simulation (the shaded region displays one standard deviation above and below the dipolarity values). Connected circles display global palaeomagnetic field model reconstructions (GGF100k, LSMOD.2, CALS10k.1b) and connected triangles present statistical GGP models (TK03, BCE19, BB18). Connected diamonds show the historical field models gufm1 and IGRF-13. For further details on these observational models, see Section 3.1. Note that the dipolarities of the palaeomagnetic field models, which are well resolved up to $\ell = 4$, saturate for degrees $\ell \geq 4$ as expected.

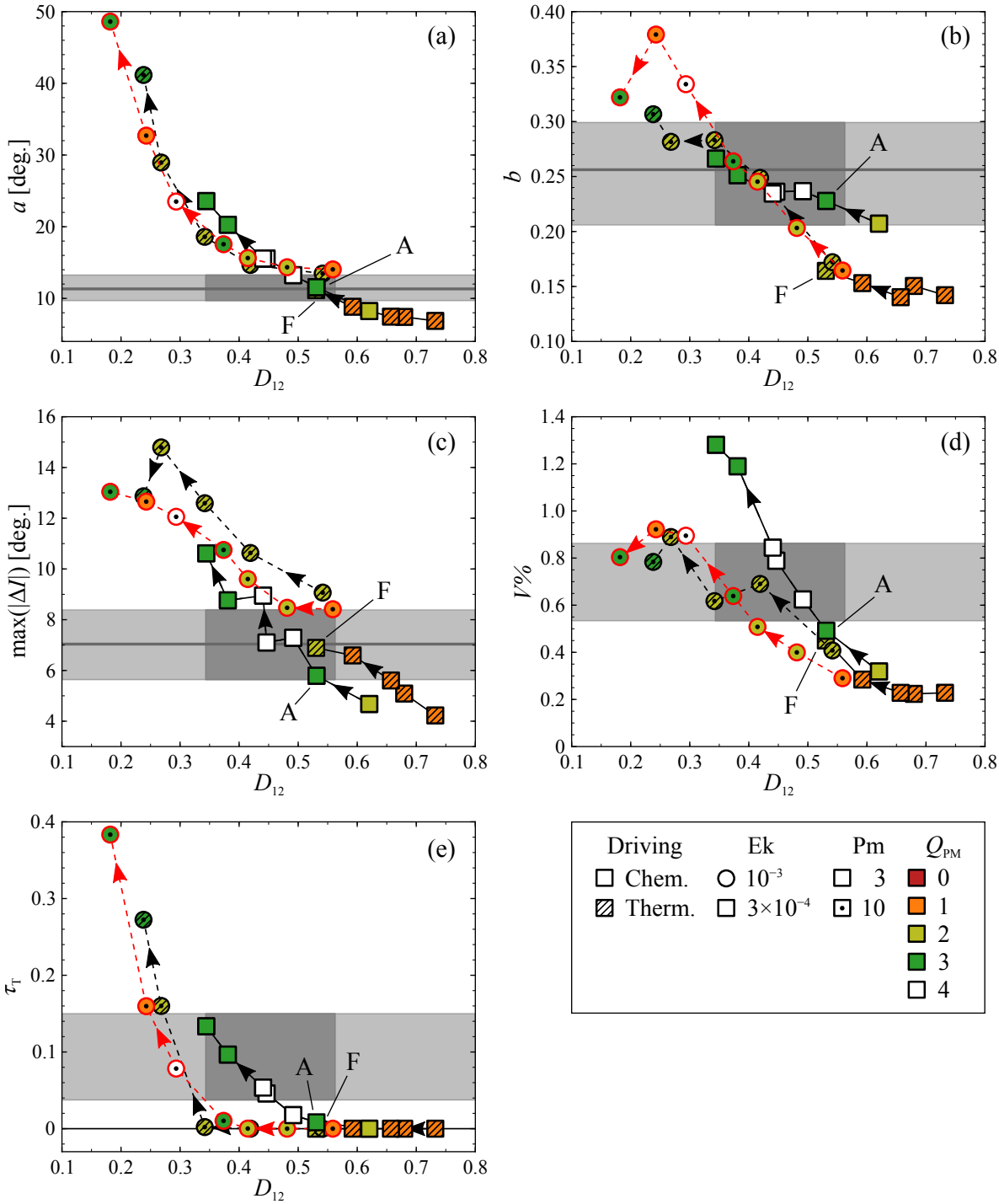

Figure S3: Same as Figure 2 but for two representative Rayleigh number tracks of the chemical and the thermal dynamos. See the legend at the bottom right for the meaning of the symbols and Figure 1 for additional information on the tracks shown and on runs A and F.

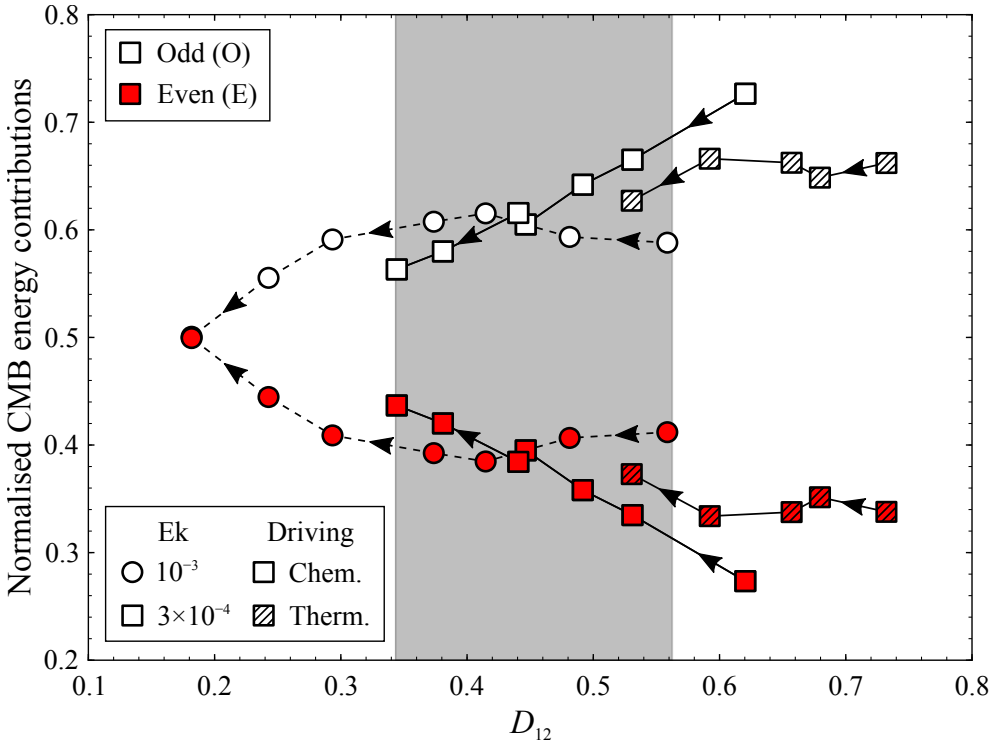

Figure S4: Normalised equatorially symmetric (even, E) and non-dipolar equatorially antisymmetric (odd, O) magnetic energy at the CMB as a function of the dipolarity D_{12} for the three Rayleigh number tracks shown in Figure 3. E (O) is defined as the ratio of the time-averaged mean CMB energy in the $\ell + m$ even (odd, excluding the axial dipole) spherical harmonics of degrees $1 \leq \ell \leq 10$ to the time-averaged total mean CMB energy in these degrees (excluding the axial dipole). We recall that the axial dipole does not contribute to VGP dispersion.

Table S1: Control parameters and time-averaged properties of the numerical geodynamo simulations explored in this study. Column 1 lists the model name: the prefix MAG (LED) refers to a simulation performed using the MagIC (Leeds) code (runs A–F are the selected cases discussed in the main article). 28 of these simulations were reported in previous studies (see the references listed in column 2: WM16 for Wicht and Meduri (2016) and S19 for Sprain et al. (2019); the model name assigned in these studies is given in parenthesis). The system control parameters, defined in Sections 2.1 and S1, are: the Ekman number Ek, the Rayleigh number Ra and the magnetic Prandtl number Pm (columns 3 to 5); the Prandtl number Pr is 1 and the shell aspect ratio is $\chi = 0.35$ in all simulations. Column 6 details the convective driving mode (chemical or thermal). Column 7 lists the codensity boundary conditions (BCs): fixed codensity (C) or fixed codensity flux (F), with the first (second) letter referring to the inner (outer) boundary. $\epsilon = (q_{\max} - q_{\min})/\langle q \rangle$ is the amplitude of the lateral heat flux variations imposed at the outer boundary, which is given in column 8. Here $q_{\min}$, $q_{\max}$ and $\langle q \rangle$ are the minimum, maximum and mean outer boundary heat flux, respectively. The heat flux pattern is a recumbent spherical harmonic of degree $\ell = 2$ and order $m = 0$. $\epsilon = 0$ refers to a homogeneous outer boundary. Column 9 lists the magnetic BCs: electrically insulating (I) or conducting (C), with the first (second) letter referring to the inner (outer) boundary. t_{sim} is the total simulation time (in units of the outer core magnetic diffusion time d^2/η; column 10). Columns 11 and 12 list the dipolarity D_{12} and D_4 respectively. Column 13 details the relative transitional time τ_{T}. The reversing regime (column 14) is defined using τ_{T} as in S19: stable dipolar (D) for $\tau_{\text{T}} < 0.0375$, reversing (R) for $0.0375 \leq \tau_{\text{T}} \leq 0.15$, multipolar (M) for $\tau_{\text{T}} > 0.15$. The last column lists the magnetic Reynolds number $\text{Rm} = \text{U}d/\eta$, where U is the time-averaged RMS core flow velocity. We note here that S19 reported a wrong Rm for LEDA021 (Model 8 in S19). File uploaded separately (TableS1.xlsx).

Table S2: Estimated Q_{PM} observables of Earth for the last 10 Myr (from Sprain et al., 2019). Median values and 95% confidence intervals of a, b, and $\max(|\Delta I|)$ are obtained from a bootstrapping technique. A range is instead estimated for $V\%$ and τ_{T}. The lower (upper) bound of $V\%$ comes from the median value of the VDM distribution in the interval $0-1$ Ma ($1-10$ Ma) of the PINT database. The number of reversals observed since 10 Ma (≈ 50, obtained from the geomagnetic polarity timescale of Ogg, 2012), an excursion rate of 10 Myr^{-1}, and an average event duration of 2.5 kyr (10 kyr) define the lower (upper) bound of τ_{T}. See Sprain et al. (2019) for further details.

a [°]	b	$\max(\lvert\Delta I\rvert)$ [°]	$V\%$	τ_{T}
$11.33^{+1.93}_{-1.63}$	$0.256^{+0.043}_{-0.050}$	$7.04^{+1.35}_{-1.40}$	$0.534-0.863$	$0.0375-0.15$

Table S3: Least-squares regression coefficients of the quadratic fits (i) $\Delta Q_{\mathrm{PM}} = c_0 + c_1 D_{12} + c_2 (D_{12})^2$ and (ii) $\Delta Q_{\mathrm{PM}} = c_0 + c_1 D_4 + c_2 (D_4)^2$ shown in Figure 1. The last column lists the coefficient of determination R^2.

Fit	Figure	c_0	c_1	c_2	R^2
(i)	1a	32.4	−128.6	142.0	0.85
	1b	32.0	−114.1	118.9	0.79
(ii)	1c	65.2	−180.8	132.0	0.85
	1d	45.6	−120.3	89.5	0.84

Table S4: Dipolarity D_{12}, modified dipolarity D_4 and Q_{PM} metrics for the simulation runs A–F and the observational field models discussed in the main article. Column 2 lists the time interval spanned. In the numerical simulations, time is rescaled assuming a magnetic diffusion time $d^2/\eta = 234$ kyr based on the electrical conductivity of Pozzo et al. (2012). Columns 3 and 4 report D_{12} and D_4 respectively, with errors denoting standard deviations. Columns 5 to 8 list median values of the equatorial VGP dispersion a and latitudinal VGP dispersion b, the maximum absolute inclination anomaly $\max(|\Delta I|)$, and the variability of the VDM distribution $V\%$ respectively (errors denote 95% confidence intervals). Column 9 details the relative transitional time τ_{T}. Columns 10 to 15 report misfits for each of these observables and the total misfit ΔQ_{PM}. All measures are dimensionless except a and $\max(|\Delta I|)$ which are given in degrees.

Model	Time interval	D_{12}	D_4	a [°]	b	$\max(\lvert\Delta I\rvert)$ [°]	$V\%$	τ_{T}	Misfit					
									a	b	ΔI	$V\%$	τ_{T}	ΔQ_{PM}
Run A	8.3 Myr	0.53 ± 0.09	0.77 ± 0.10	$11.56^{+0.80}_{-0.77}$	$0.23^{+0.03}_{-0.03}$	$5.8^{+3.2}_{-3.1}$	$0.49^{+0.03}_{-0.03}$	0.008	0.09	0.37	0.27	1.08	1.51	3.32
Run B	8.6 Myr	0.49 ± 0.11	0.74 ± 0.13	$13.24^{+1.06}_{-1.02}$	$0.24^{+0.04}_{-0.04}$	$7.3^{+4.0}_{-3.6}$	$0.62^{+0.03}_{-0.03}$	0.018	0.65	0.22	0.05	0.37	1.34	2.63
Run C	5.2 Myr	0.45 ± 0.13	0.69 ± 0.16	$15.57^{+1.46}_{-1.27}$	$0.24^{+0.05}_{-0.05}$	$7.1^{+4.6}_{-4.1}$	$0.79^{+0.04}_{-0.04}$	0.046	1.32	0.19	0.01	0.44	0.80	2.77
Run D	20.3 Myr	0.39 ± 0.14	0.65 ± 0.19	$16.92^{+1.89}_{-1.74}$	$0.24^{+0.07}_{-0.08}$	$7.3^{+5.3}_{-5.0}$	$0.91^{+0.05}_{-0.05}$	0.065	1.53	0.14	0.04	1.00	0.52	3.23
Run E	13.6 Myr	0.37 ± 0.07	0.62 ± 0.10	$17.56^{+1.13}_{-1.05}$	$0.26^{+0.04}_{-0.05}$	$10.8^{+4.5}_{-4.3}$	$0.64^{+0.03}_{-0.03}$	0.010	2.09	0.09	0.65	0.30	1.48	4.61
Run F	3.7 Myr	0.53 ± 0.06	0.80 ± 0.07	$11.16^{+0.63}_{-0.61}$	$0.16^{+0.02}_{-0.03}$	$6.9^{+1.2}_{-1.2}$	$0.45^{+0.02}_{-0.02}$	0	0.07	1.25	0.06	1.33	1.67	4.37
TK03	-	0.56 ± 0.14	0.79 ± 0.14	$10.95^{+0.97}_{-0.86}$	$0.24^{+0.03}_{-0.03}$	$2.44^{+3.23}_{-2.91}$	$0.51^{+0.03}_{-0.03}$	0.007	0.15	0.18	0.99	1.01	1.54	3.87
BCE19	-	0.56 ± 0.14	0.79 ± 0.14	$10.14^{+0.98}_{-0.87}$	$0.25^{+0.03}_{-0.03}$	$2.22^{+3.21}_{-2.73}$	$0.50^{+0.03}_{-0.03}$	0.004	0.46	0.10	1.05	1.03	1.59	4.23
BB18	-	0.54 ± 0.18	0.76 ± 0.18	$12.53^{+1.35}_{-1.23}$	$0.27^{+0.05}_{-0.05}$	$2.27^{+3.92}_{-3.65}$	$0.64^{+0.03}_{-0.03}$	0.035	0.38	0.12	0.90	0.29	1.05	2.74
GGF100k	$0 - 100$ ka	-	0.84 ± 0.08	-	-	-	-	0	-	-	-	-	-	-
LSMOD.2	$30.1 - 49.9$ ka	-	0.74 ± 0.18	-	-	-	-	0.030	-	-	-	-	-	-
CALS10k.1b	$0 - 10$ ka	-	0.92 ± 0.04	-	-	-	-	0	-	-	-	-	-	-
gufm1	$1582 - 1987$ AD	0.79 ± 0.06	0.88 ± 0.03	-	-	-	-	0	-	-	-	-	-	-
IGRF-13	$1900 - 2020$ AD	0.69 ± 0.03	0.82 ± 0.02	-	-	-	-	0	-	-	-	-	-	-

Table S5: Additional summary simulation outputs used to construct Figures 1–3 in the main article. Columns 2 to 5 report median values of the equatorial VGP dispersion a (in degrees) and latitudinal VGP dispersion b, the maximum absolute inclination anomaly $\max(|\Delta I|)$ (in degrees), and the variability of the VDM distribution $V\%$ respectively. Columns 6 to 10 list misfits of a, b, $\max(|\Delta I|)$, $V\%$, and τ_{T} respectively. The total misfit ΔQ_{PM} and total score Q_{PM} are given in columns 11 and 12, respectively. The last two columns detail the time-averaged dipole field strength at the CMB, $\overline{B}_{\mathrm{d}}$, and its standard deviation σ_{d} in units of $(\rho\mu_0\Omega\eta)^{1/2}$. File uploaded separately (TableS5.xlsx).